

Properties of HI discs in the Auriga cosmological simulations

Federico Marinacci^{1*}, Robert J. J. Grand^{2,3}, Rüdiger Pakmor², Volker Springel^{2,3},
Facundo A. Gómez⁴, Carlos S. Frenk⁵ and Simon D. M. White⁴

¹*Kavli Institute for Astrophysics and Space Research, Massachusetts Institute of Technology, Cambridge, MA 02139, USA*

²*Heidelberger Institut für Theoretische Studien, Schloss-Wolfsbrunnengasse 35, 69118 Heidelberg, Germany*

³*Zentrum für Astronomie der Universität Heidelberg, ARI, Mönchhofstrasse 12-14, 69120 Heidelberg, Germany*

⁴*Max-Planck-Institut für Astrophysik, Karl-Schwarzschild-Str. 1, D-85748, Garching, Germany*

⁵*Institute for Computational Cosmology, Department of Physics, Durham University, South Road, Durham, DH1 3LE, UK*

23 April 2022

ABSTRACT

We analyse the properties of the HI gas distribution in the Auriga project, a set of magnetohydrodynamic cosmological simulations performed with the moving-mesh code AREPO and a physics model for galaxy formation that succeeds in forming realistic late-type galaxies in the 30 Milky Way-sized haloes simulated in this project. We use a simple approach to estimate the neutral hydrogen fraction in our simulation set, which treats low-density and star-forming gas separately, and we explore two different prescriptions to subtract the contribution of molecular hydrogen from the total HI content. The HI gas in the vast majority of the systems forms extended discs although more disturbed morphologies are present. Notwithstanding the general good agreement with observed HI properties – such as radial profiles and the mass-diameter relation – the Auriga galaxies are systematically larger and more gas-rich than typical nearby galaxies. Interestingly, the amount of HI gas outside the disc plane correlates with the star formation rate, consistent with a picture where most of this extra-planar HI gas originates from a fountain-like flow. Our findings are robust with respect to the different assumptions adopted for computing the molecular hydrogen fraction and do not vary significantly over a wide range of numerical resolution. The HI modelling introduced in this paper can be used in future work to build artificial interferometric HI data cubes, allowing an even closer comparison of the gas dynamics in simulated galaxies with observations.

Key words: galaxies: evolution – galaxies: ISM – galaxies: fundamental properties – galaxies: structure – methods: numerical

1 INTRODUCTION

(Cold) gas plays a key role in the evolution of galaxies, in particular in those that are still actively forming stars like our own Milky Way. Indeed, the presence of a cold gas reservoir is necessary for a galaxy to keep forming stars (e.g. [Sancisi et al. 2008](#), and references therein). Moreover, several pieces of evidence ([Twarog 1980](#); [Chiappini et al. 1997, 2001](#); [Aumer & Binney 2009](#)) indicate that some process of accretion, replacing the gas consumed by star formation with fresh (and possibly metal-poor) material, must be ongoing for a substantial fraction of the lifetime of a star-forming galaxy.

A very important component of this cold gas phase is represented by atomic hydrogen (HI). Radio observations of HI in nearby galaxies now date back several decades ([Roberts 1975](#)) and have been instrumental to study the kinematics (e.g. [Verheijen & Sancisi 2001](#)), structure (e.g. [Broeils & Rhee 1997](#)) and gaseous content (e.g. [Catinella et al. 2013](#)) of (late-type) galaxies (see also

[Giovannelli & Haynes 2016](#), for an updated review on HI surveys). As the sensitivity of these observations improved with time ([Heald et al. 2011](#); [Kalberla et al. 2005](#); [Wang et al. 2013](#)), it has become possible to detect fainter and fainter HI structures, which has not only allowed a better census of the total HI content in spiral galaxies but also elucidated the interactions they have with their environment and their importance for galactic evolution. For example, the detection of extra-planar gas layers (i.e. low-column density HI gas that extends well outside the plane of the galactic disc, see e.g. [Oosterloo et al. 2007](#)) and the study of their kinematics ([Fraternali 2009](#), and references therein) has revealed the interplay between the disc and the circumgalactic medium in late-type galaxies ([Fraternali & Binney 2008](#); [Marinacci et al. 2010, 2011](#)). This interaction is mediated by a so-called galactic fountain ([Shapiro & Field 1976](#); [Houck & Bregman 1990](#)) – which in the Milky Way manifests itself through intermediate-velocity (IVC) and high-velocity (HVC) clouds ([Fraternali et al. 2015](#); [Marasco & Fraternali 2011](#); [Wakker & van Woerden 1997](#); [Wakker 2004](#)) – and provided indi-

* E-mail: fmarinac@mit.edu

rect evidence of how star formation can be sustained for a Hubble time in these systems (Fraternali 2014).

The reproduction of the content and distribution of HI gas in theoretical models of galaxy formation is of primary importance, given its key role in shaping galactic evolution. In fact, the numerous constraints posed by such observations represent a challenging test for any galaxy formation model. This is particularly true in hydrodynamical simulations, in which, due to the huge dynamic range in spatial scales that needs to be covered, many of the physical processes crucial for forming realistic objects are included in an approximate sub-grid fashion. The latter may in principle introduce a substantial uncertainty in the final results, and also an explicit dependence on the details of the numerical implementation of the sub-grid processes, calling for a validation against observations.

Some work in this direction has already been carried out, both in idealized set-ups and in full cosmological settings. These efforts mostly focused on the dependence on supernova feedback – a key process in galaxy formation models, especially for galaxies with virial masses up to $\sim 10^{12} M_{\odot}$ – of the extra planar HI distribution and kinematics in idealized Milky Way type galaxies (Marasco et al. 2015), and of the global HI properties in full cosmological set-ups (e.g. Davé et al. 2013; Popping et al. 2009; Rahmati et al. 2013; Walker et al. 2014). However, the majority of this earlier cosmological work featured a simulated galaxy population with properties that are in substantial tension with observations, even when matching the large-scale HI observational constraints. In particular, the simulated galaxies invariably exhibited too high stellar masses and lacked a well-defined disc component, due to an overly efficient cooling of baryons at the centre of dark matter haloes (the so-called ‘over-cooling’ problem, e.g. Navarro & Steinmetz 1997).

It was not until recently that this issue has been successfully addressed, essentially by invoking a more efficient coupling of the feedback energy – both stellar and, at the high $\gtrsim 10^{12} M_{\odot}$ mass end, from active galactic nuclei – with the cooling gas. This more effective coupling can be very difficult to numerically resolve in full-scale cosmological simulations, and different groups have explored various approaches to address this problem. Notwithstanding these technical difficulties, there are now several simulation methodologies that are able to produce realistic looking galaxies in hydrodynamic cosmological simulations both in uniformly-sampled boxes – as for instance in the Illustris (Vogelsberger et al. 2014a,b) and EAGLE (Schaye et al. 2015) simulation projects – and in zoom-in configurations that focus on the formation of a single object (e.g. Aumer et al. 2013; Colín et al. 2016; Guedes et al. 2011; Marinacci et al. 2014a; McCarthy et al. 2012; Stinson et al. 2013; Wang et al. 2015), commonly a Milky Way-sized galaxy.

The availability of a new generation of cosmological simulations yielding realistic galaxies implies that it is now possible to study their HI content and kinematics more reliably than possible in the past (for very recent analysis see Crain et al. 2016; Macciò et al. 2016; Marasco et al. 2016), and also to check whether the increased feedback efficiency, which nominally should significantly affect the gas properties within and in the vicinity of the star-forming disc, has an effect on the (global) distribution of the HI gas. This has been explored in the context of the EAGLE collaboration by Bahé et al. (2016, hereafter B16), who have analysed several properties of the HI gas – including morphologies, radial distribution, gas fractions, HI masses and sizes – of the simulated galaxy set. In their study, B16 conclude that the increased efficiency of the stellar feedback and its local character have indeed a large impact on the morphology of the HI discs, and strongly influences its radial

distribution. Other properties, such as HI masses and sizes, appear to be less sensitive to the increased (stellar) feedback efficiency.

Similarly to the work of B16, in this paper we present an analysis of the HI properties of a set of 30 cosmological zoom-in MHD simulations of disc galaxy formation, named the Auriga simulations, performed with the moving-mesh code AREPO and a state-of-the-art model of galaxy formation physics largely based on the one used for the Illustris project (see Vogelsberger et al. 2013), slightly adapted for zoom-in simulations of Milky Way type objects (Marinacci et al. 2014a). Compared to the study of B16 the zoom-in technique makes it possible to reach a finer (mass and spatial) resolution, and the relatively large number of simulated haloes allows us to draw statistically meaningful conclusions about the properties of the resulting HI discs, albeit limited to halo masses around $\simeq 10^{12} M_{\odot}$ which is the range of masses chosen as Milky Way-like candidate haloes in the Auriga project. We note that the B16 and our simulation set have very different treatments for the star-forming gas and stellar feedback, enabling an interesting comparison on how the numerical implementation of these aspects impacts the simulated HI distribution.

This paper is structured as follows. In Section 2, we briefly describe the main properties of the simulations that we have analysed in this study and the numerical techniques employed to carry them out. Section 3 presents the method that we have adopted to estimate the HI content of the Auriga discs, and in particular gives details on the two prescriptions that we have used to treat the molecular gas fraction. In Section 4, we illustrate our main results focusing on the structural properties, scaling relations and gas content of the simulated HI discs. These findings are compared to observations and with previous simulation results. Finally, in Section 5, we present our conclusions.

2 THE AURIGA SIMULATIONS

In this work, we investigate the HI content of the cosmological hydrodynamical simulation suite Auriga (Grand et al. 2016a). This simulation suite is aimed at modelling the formation and evolution of Milky Way-like galaxies in their proper cosmological context. Full technical details about the simulation suite can be found in Grand et al. (2016a)¹. In the following, we restrict ourselves to a concise description of the numerical methods adopted to run the simulations and their main properties.

The Auriga simulations follow a Λ CDM cosmology with parameters $\Omega_m = \Omega_{\text{dm}} + \Omega_b = 0.307$, $\Omega_b = 0.048$, $\Omega_{\Lambda} = 0.693$, and Hubble constant $H_0 = 100 h \text{ km s}^{-1} \text{ Mpc}^{-1} = 67.77 \text{ km s}^{-1} \text{ Mpc}^{-1}$, consistent with the Planck Collaboration XVI (2014) data release. The candidate haloes selected for resimulation were identified in a low-resolution simulation of a periodic cosmological box of side 100 Mpc. Candidate haloes were selected in a virial mass range around $10^{12} M_{\odot}$, consistent with recent determinations of the MW mass (Wilkinson & Evans 1999; Sakamoto et al. 2003; Battaglia et al. 2005; Dehnen et al. 2006; Li & White 2008; Xue et al. 2008; Peñarrubia et al. 2016), a mild isolation criterion – no object of more than half the mass of the candidate is allowed to be closer than 1.37 Mpc – was enforced at $z = 0$ to select relatively isolated objects.

The selected haloes (denoted with the acronym Au i , where

¹ For more information about the simulation suite see also the project’s website <http://auriga.h-its.org>

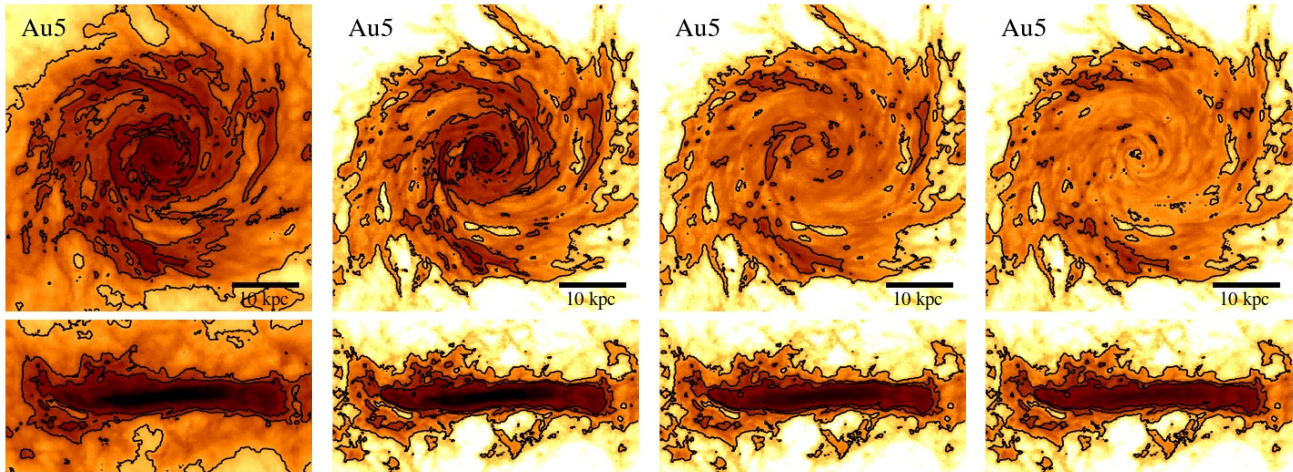


Figure 1. H I projections. From left to right: total H density, neutral H density (H I + H₂), H I density from the L08 pressure prescription, H I density from the GK11 prescription. The size of the projected region is 50 kpc on a side for face on projections and 50 × 25 kpc for edge-on projections. To align the projections, the spin direction of the cold, star-forming gas within 10% of the virial radius of the halo has been used. The colour scale logarithmically maps the column densities in the interval $[5 \times 10^{18}, 10^{22}] \text{ cm}^{-2}$, and contour levels are placed at 10, 5 and 1 $M_{\odot} \text{ pc}^{-2}$ from the inside to the outside.

i is the halo id) were simulated multiple times at different resolution levels by applying the so-called “zoom-in” technique, in which the mass distribution in the Lagrangian region that forms the main halo is sampled by a large number of resolution elements, whereas progressively coarser resolution is applied with increasing distance from the target object. At the fiducial resolution level that we are going to analyse in the present work (which from now on will be referred to as level 4), the typical baryonic mass resolution is $\sim 4 \times 10^4 M_{\odot}$ and that of the dark matter component is $\sim 3 \times 10^5 M_{\odot}$. The softening length of the dark matter particles is kept fixed in comoving space and allowed to grow in physical space up to a maximum of 369 pc, while the gas softening length is scaled by the mean radius of the cell. The maximum physical softening allowed is 1.85 kpc.

Gas was included in the initial conditions by adopting the same technique as in Marinacci et al. (2014a,b, and references therein). In practice, each particle in the initial conditions is split into a pair of a dark matter particle and a gas cell. The phase space coordinates of the pair are chosen such that its centre of mass and centre of mass velocity are equal to those of the original dark matter particle. The mass ratio of the pair is set by the cosmic baryon fraction, and the dark matter particle and gas cell are separated by a distance equal to half the mean inter-particle spacing.

The simulation suite was carried out using the moving-mesh, magneto-hydrodynamics code AREPO (Springel 2010). To solve for collisionless dynamics, AREPO employs a TreePM approach, in which the gravitational force is split into a long-range and a short-range component (see Springel 2005, for details). The long-range contribution is calculated on a Cartesian mesh via a Fourier method, while for the short-range component a gravitational oct-tree (Barnes & Hut 1986) is used. The magnetohydrodynamic (MHD) equations are discretized in a finite-volume approach on a dynamic unstructured Voronoi tessellation of the simulation domain. The special trait of AREPO, distinguishing it from other cosmological finite-volume codes, is that the mesh-generating points defining the Voronoi tessellation are allowed to move with the local fluid velocity, thereby giving rise to a quasi-Lagrangian numerical method which is manifestly Galilean-invariant. The MHD equations are solved with a second order Runge-Kutta integration

scheme complemented with least square spatial gradient estimators of primitive variables (Pakmor et al. 2016) and the Powell et al. (1999) 8-wave cleaning scheme to ensure the $\nabla \cdot \mathbf{B} = 0$ constraint.

The Auriga simulations use a galaxy formation physics model that accounts for the baryonic processes that play a key role in the formation of late-type galaxies. The model itself is an updated version of the one used in Marinacci et al. (2014a,b), which was specifically developed for large-scale cosmological simulations and whose free parameters were calibrated against a small set of observables such as the cosmic star formation history and the galaxy stellar mass function. For a full description of the implementation details we refer the reader to Vogelsberger et al. (2013). Differences of the present galaxy formation module with respect to the Marinacci et al. (2014a) implementation are discussed in Grand et al. (2016a).

Magnetic fields are included in the initial conditions as in Pakmor et al. (2014) by seeding a homogeneous B -field of 10^{-14} (co-moving) G along the z -direction, which is then amplified due to the assembly of the main galaxy. The seeding is necessary because, in ideal MHD, B -fields cannot be self-consistently generated when starting from zero-field initial conditions. We note that previous cosmological MHD simulations with AREPO have shown that the results are essentially insensitive to the choice of both the intensity and the direction of the seed field (Pakmor et al. 2014), at least inside virialized structures (Marinacci et al. 2015) where any memory of the initial conditions is quickly erased due to vigorous, small-scale dynamo amplification of the field.

3 COMPUTATION OF THE H I MASS

The first step in our analysis is to estimate the amount of neutral atomic hydrogen contained in any given cell ($M_{\text{HI},i}$) of our simulated objects, which can be expressed as follows

$$M_{\text{HI},i} = (1 - f_{\text{mol},i}) f_{\text{neutr},i} X_i M_i, \quad (1)$$

where M_i is the total gas mass contained in a given cell i , X_i is the hydrogen mass fraction, $f_{\text{neutr},i}$ the neutral hydrogen fraction and $f_{\text{mol},i}$ the molecular hydrogen fraction, respectively. M_i and X_i are

readily available from the simulation output, since AREPO directly tracks their evolution. The determination of the neutral H fraction $f_{\text{neutr},i}$ and of the molecular H fraction $f_{\text{mol},i}$ is, however, slightly more involved and require some additional modelling. We discuss the procedure that we have adopted to estimate these quantities in the subsections below.

3.1 Estimate of the neutral gas fraction $f_{\text{neutr},i}$

The gas cooling module in AREPO determines $f_{\text{neutr},i}$ for each cell, and this information could in principle be directly used in eq. (1). However, in the galaxy formation model used in the simulations, gas above a predetermined density threshold, $n_{\text{th}} \sim 0.13 \text{ cm}^{-3}$, is eligible for star formation. This star-forming gas, in turn, is modelled by an effective equation of state describing a simplified ISM model comprised of hot ($T \sim 10^7 \text{ K}$) and cold ($T \sim 10^3 \text{ K}$) gas phases in pressure equilibrium (see [Springel & Hernquist 2003](#)). Because the thermodynamic state of the gas is dictated by the effective equation of state, the value $f_{\text{neutr},i}$ estimated by the code for the star-forming gas is unreliable for our purposes.

As stated above, the cold gas phase, which is one of the constituents of our ISM model, has a temperature around 10^3 K and as such we expect that the gas comprising it is essentially neutral. Therefore, it is natural to assume that for star-forming gas, $f_{\text{neutr},i}$ is simply the mass fraction of the cold gas phase of our ISM, which can be easily determined as (see [Springel & Hernquist 2003](#))

$$x = \frac{u_h - u}{u_h - u_c}, \quad (2)$$

where $u = P/[(\gamma - 1)\rho]$ is the gas thermal energy per unit mass (set by the effective equation of state), and u_c and u_h are the gas thermal energy of the cold and the hot ISM phase, respectively. In what follows we will thus use for $f_{\text{neutr},i}$ the value estimated from eq. (2) if the gas is star-forming, or otherwise the value directly computed by the AREPO cooling module for gas densities below the star formation threshold n_{th} .

3.2 Treatment of the molecular gas

Once $f_{\text{neutr},i}$ has been determined, the contribution of the atomic hydrogen must be separated from the molecular phase. The galaxy formation physics modules currently employed in AREPO do not directly account for the mechanisms responsible for the creation and destruction of molecular hydrogen. Therefore, we adopt two phenomenological methods to achieve this objective, also with the goal to investigate systematic differences arising from the specific treatment of molecular hydrogen in our analysis (see Section 4 for more details).

The first method is purely empirical and is based on a set of observations of nearby galaxies ([Leroy et al. 2008](#), hereafter [L08](#)). As originally proposed by [Blitz & Rosolowsky \(2006\)](#), it consists of fitting the ratio R_{mol} between the column density of molecular over atomic hydrogen with the functional form

$$R_{\text{mol}} = \left(\frac{P}{P_0} \right)^\alpha, \quad (3)$$

where P is the gas mid-plane pressure and P_0 and α are free parameters. In our case, we assume that R_{mol} in eq. (3) is the ratio between the molecular and atomic hydrogen and P the gas pres-

sure² in any given cell. The molecular fraction can then be easily obtained as

$$f_{\text{mol},i} = \frac{R_{\text{mol},i}}{R_{\text{mol},i} + 1}, \quad (4)$$

once the value of P_0 and α have been fixed. Following [L08](#) we choose $P_0 = 1.7 \times 10^4 \text{ K cm}^{-3}$ and $\alpha = 0.8$. We explicitly checked that using the parametrization proposed by [Blitz & Rosolowsky \(2006\)](#) does not alter our findings significantly.

The second method is more theoretically motivated and is based on the work by [Gnedin & Kravtsov \(2011\)](#), hereafter [GK11](#). Following [Lagos et al. \(2015, Appendix A1\)](#) we define

$$f_{\text{mol},i} = \left(1 + \frac{\Sigma_c}{\Sigma_{\text{neutr},i}} \right)^2, \quad (5)$$

where $\Sigma_{\text{neutr},i}$ is the neutral hydrogen column density and Σ_c is a critical column density given by

$$\Sigma_c = 20 \text{ M}_\odot \text{ pc}^{-2} \frac{\Lambda(D_{\text{MW}}, G'_0)^{4/7}}{D_{\text{MW}} \sqrt{1 + G'_0 D_{\text{MW}}^2}}. \quad (6)$$

In the previous expression, D_{MW} is the dust-to-gas mass ratio normalized to the Milky Way value and estimated as $D_{\text{MW}} \equiv Z_i/Z_\odot$, where Z_i is the metallicity of the gas cell in solar units ($Z_\odot = 0.0127$), G'_0 is the interstellar radiation field in units of the [Habing \(1968\)](#) radiation field, and $\Lambda(D_{\text{MW}}, G'_0)$ is a fitting function depending on the latter two variables (see [GK11](#); [Lagos et al. 2015](#), for more details). As in [Lagos et al. \(2015\)](#), G'_0 is expressed in terms of the star formation rate density in the solar neighbourhood as $G'_0 = \Sigma_{\text{SFR}}/\Sigma_{\text{SFR},0}$, where $\Sigma_{\text{SFR},0} = 10^{-3} \text{ M}_\odot \text{ yr}^{-1} \text{ kpc}^{-2}$ ([Bonatto & Bica 2011](#)). Column (surface) densities are computed by multiplying the relevant volumetric quantities by the Jeans length (see [Schaye 2001](#))

$$\lambda_J = \frac{c_s}{\sqrt{G\rho}}, \quad (7)$$

where c_s is the sound speed, G the gravitational constant, and ρ the total gas density. λ_J is computed individually for every cell. Finally, to protect against numerical divergences, a metallicity floor equal to $10^{-8} Z_\odot$ is imposed.

Figure 1 illustrates the different steps of the procedure that we have just described when applied to halo Au 5. In particular, the panels from left to right can be thought of as the result of progressively applying the correcting factors (from the rightmost to the leftmost) used to determine the HI content listed in eq. (1) to the total gas cell mass. They show, respectively, the projection both face on (top row) and edge on (bottom row) of the total H density (including ionized gas), the neutral H density ($\text{HI} + \text{H}_2$) and the HI density obtained following the [L08](#) and [GK11](#) prescriptions.

It is readily apparent in these projections that the disc of neutral hydrogen in the Au 5 halo is surrounded by a much more extended layer of ionized gas. Removing the ionized layer leaves a gaseous disc that has about the same extent and external shape whether or not molecular hydrogen is taken into account. This is consistent with the picture that molecules form in the highest density regions (i.e. in the central regions of the simulated discs), and their importance to the mass budget contribution in the outskirts is negligible. The largest difference between the total ($\text{HI} + \text{H}_2$)

² We consider only the partial pressure of the cold gas phase for the star-forming gas

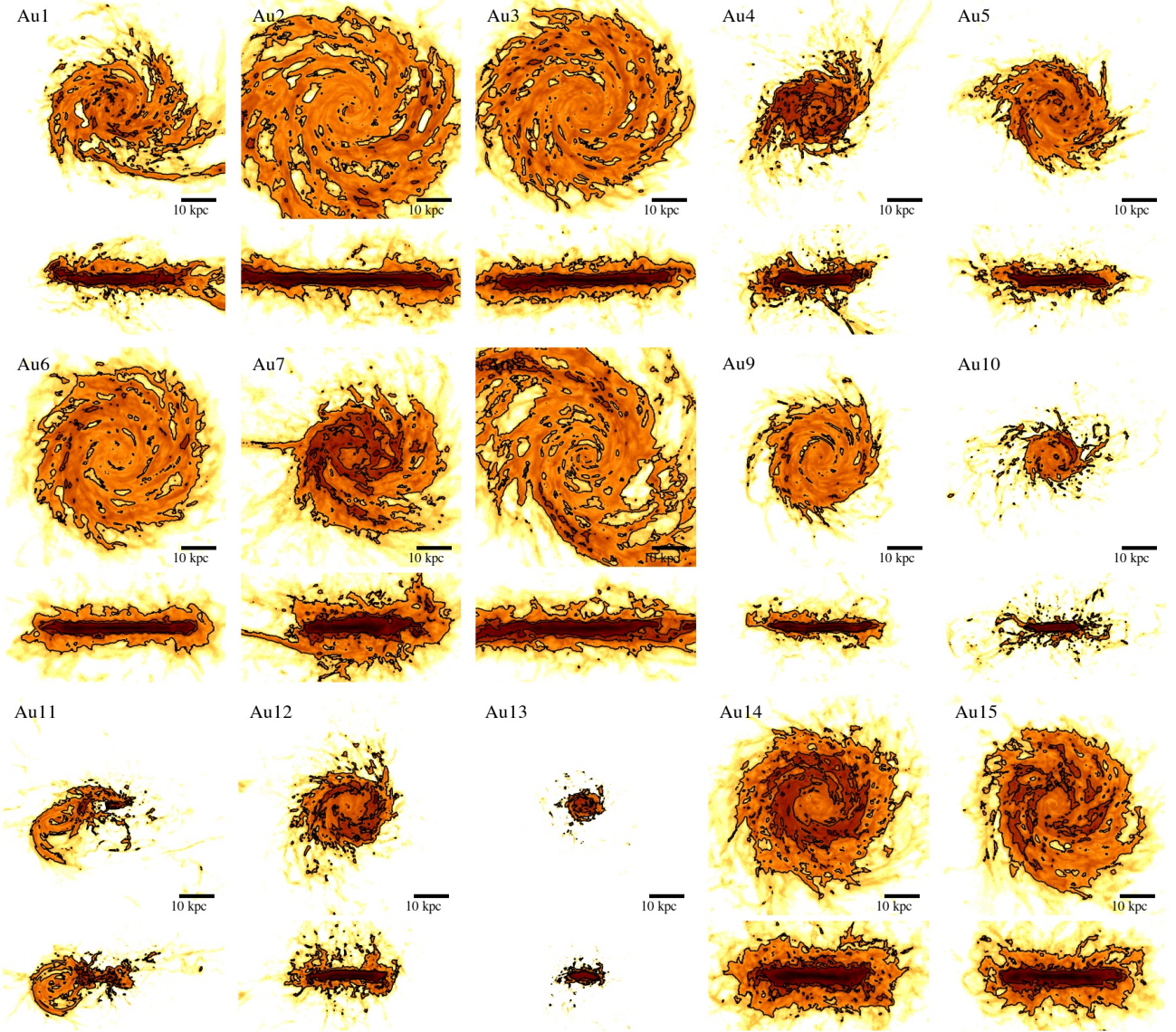


Figure 2. H I projections for haloes Au 1 to Au 15 obtained by using the [L08](#) empirical relation to account for molecular gas. Each halo is shown face-on (top) and edge-on (bottom). The size of the projection region is 90 kpc on a side for face-on projections and 90×45 kpc for the edge-on views.

neutral hydrogen and H I column density is certainly in the centre (the innermost ~ 10 kpc), where the projected density drops by a factor of ~ 10 . Although there is a very good resemblance in the main morphological features of the H I projection regardless of the method used to take into account the molecular gas, some minor differences are visible, and in particular the [GK11](#) method yields consistently lower H I column densities in the central regions of the simulated disc. As we will discuss more extensively later on, this appears to be a general trend and it is not limited to the particular halo that we have presented here.

4 RESULTS

4.1 H I morphologies

We start our analysis by presenting in Figs. 2 and 3 H I density projections for the set of 30 Auriga galaxies at redshift $z = 0$ obtained with the [L08](#) method to estimate the molecular gas fraction. Both

face-on (top panels) and edge-on projections (bottom panels) are presented. The gaseous discs are aligned by computing the spin axis of the dense, star-forming gas within 10% of the virial radius of each object. Each panel has the same physical size (90×90 kpc for face-on projections, and 90×45 kpc for the edge-on ones, with a depth of projection of 90 kpc in all cases) to facilitate the size comparison among different objects, and is centred on the potential minimum of each simulated galaxy. The colour mapping, encoding column densities in the range $5 \times 10^{18} - 10^{22} \text{ cm}^2$, is also kept the same in all panels for the same reason. Contours are placed at H I surface densities of 10, 5, and $1 \text{ M}_\odot \text{ pc}^{-2}$ from the innermost to the outermost.

In the majority of the systems, the H I gas is distributed in an extended disc (i.e. is more extended than the stellar component), which in some cases can reach galactocentric distances up to ~ 60 kpc (e.g. Au 2, Au 16, Au 24). In the vertical direction, the thickness of the H I layer is very diverse. We have examples of relatively thin gaseous discs (e.g. Au 2, Au 9, Au 10, Au 18, Au 19,

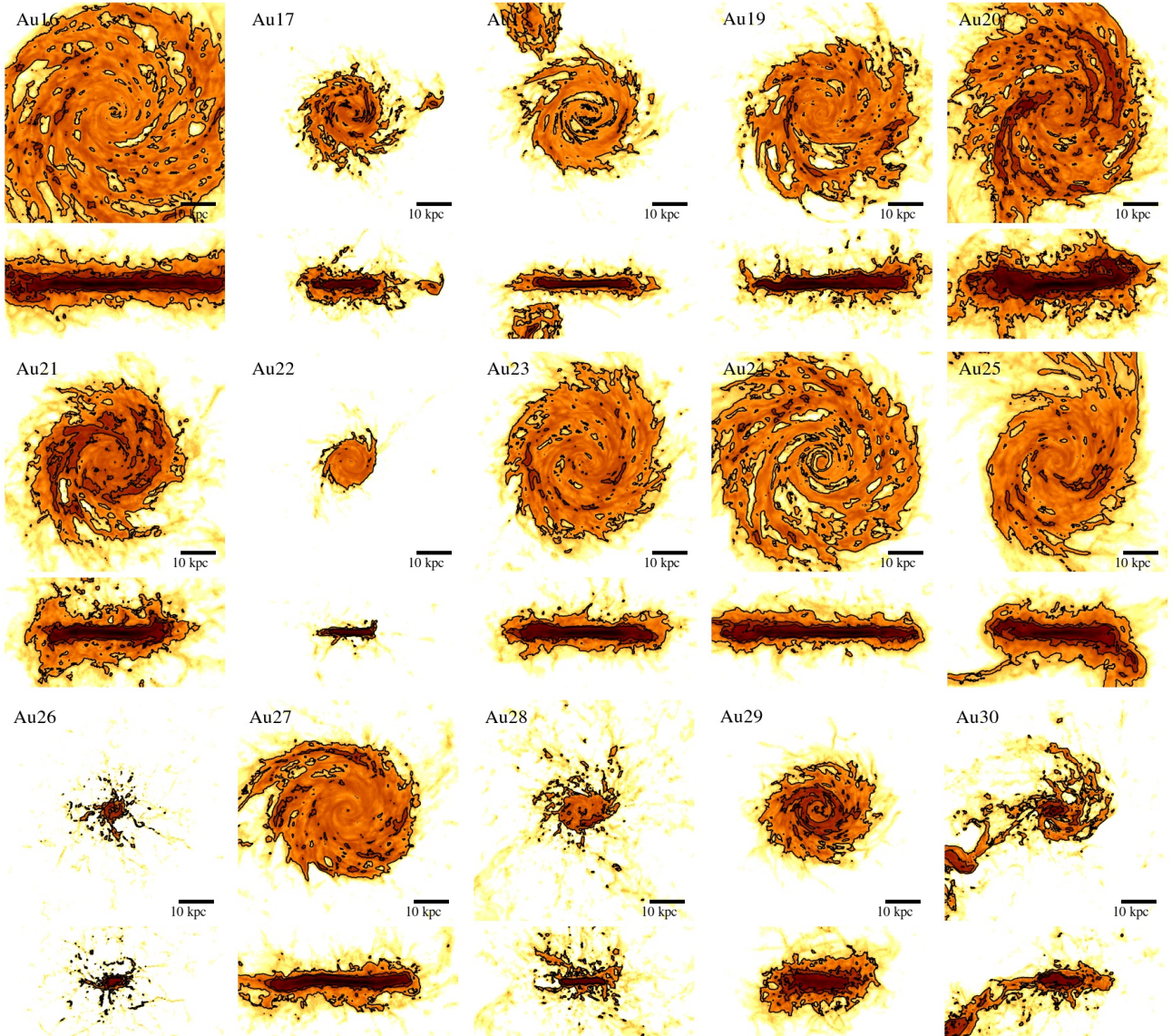


Figure 3. HI projections for haloes Au 16 to Au 30 obtained by using the [L08](#) empirical relation to account for molecular gas. Each halo is shown face on and edge on. The size of the projection region is 90 kpc on a side for face-on projections and 90×45 kpc for the edge-on views.

Au 23, Au 24) while others feature a very extended vertical distribution (Au 7, Au 14, Au 15, Au 21, Au 25, Au 29) that can reach tens of kpc outside the mid-plane. In the latter case, these vertically extended layers are often found in conjunction with a ring of more dense HI material or gas that is tracking spiral-like features in the face-on projection. These features are much less frequent (and less prominent) for thinner HI discs. In Section 4.3 we discuss the disc vertical thickness in more detail and relate it to the galactic fountain flows generated by stellar feedback.

A comparison between the HI morphologies obtained with the two prescriptions to determine the molecular gas fraction is presented in Fig. 4 (top row showing the [L08](#) method and bottom row the [GK11](#) method, respectively) for a few selected examples. In agreement with the results discussed in Sec. 3.2, the morphologies of the HI discs remain relatively unchanged. For example, their vertical and radial extent is only marginally affected by how the contribution of H_2 is calculated (see also Table 1 and Sec. 4.4 for a more quantitative analysis). The main difference is again in the central

regions of the disc, where the [GK11](#) approach predicts a lower HI fraction than the [L08](#) method. This is illustrated by the decrease of the HI surface density, which sometimes, like in Au 18 and Au 24, can be very pronounced and extend over large (~ 10 kpc) scales.

It is also informative to compare our HI morphology with that obtained in other cosmological simulations of galaxy formation, and in particular with the recent HI study of [B16](#) based on the *EAGLE* simulations ([Schaye et al. 2015](#)). An interesting aspect of this comparison is that similar methods were used to estimate the HI fraction in both the *EAGLE* and *Auriga* simulations, whereas the two simulation sets differ in the implementation of the ISM physics and stellar feedback. The main difference lies in the treatment of stellar feedback, which is local and more violent in *EAGLE* compared to the *Auriga* model. The latter employs a stochastic spawning of wind “particles” that effectively gives rise to a non-local injection of supernova momentum (see [Vogelsberger et al. 2013](#), for details). This has a significant impact on the HI morphologies. In the *EAGLE* simulations, unrealistically large holes of kpc size are

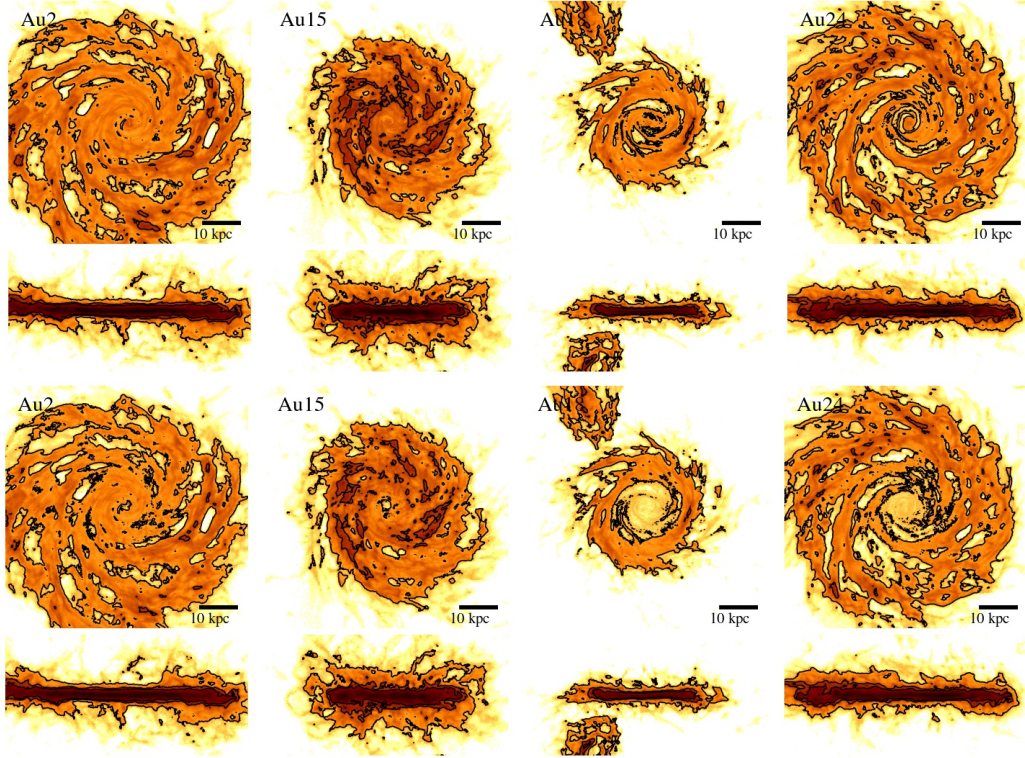


Figure 4. Comparison of the H I disc morphologies obtained by using the **L08** (top row) and **GK11** (bottom row) prescriptions to account for molecular gas for a selection of 4 Auriga haloes. Each halo is shown face-on and edge-on, with a size of the projection region of 90 kpc on a side for face-on projections and 90×45 kpc for edge-on projections.

clearly visible in the neutral gas distribution. This affects not only the morphologies of the H I discs, but also the radial gas distribution. Our simulations do not seem to suffer from the same problem, although gaps in the H I distribution can sometimes be seen, especially for the more extended H I discs (for example Au 2, Au 16, Au 24).

4.2 H I radial profiles

Figures 5 and 6 show azimuthally averaged H I surface density profiles as a function of the galactocentric radius for the 30 objects in the Auriga simulations. The galactocentric radii have all been expressed in terms of the azimuthally averaged H I radius of each object, defined as $\Sigma_{\text{HI}}(R_{\text{HI}}) = 1 \text{ M}_{\odot} \text{ pc}^{-2}$ (see, e.g., [Broeils & Rhee 1997](#), and Table 1 for their values). The profiles have been obtained by turning the H I disc face on (using again a direction defined by the angular momentum of the cold star-forming gas) and considering the gas cells in a region of 240×120 kpc centred on the halo potential minimum. The gas cells in this region have been binned in 120 concentric annuli of 1 kpc width, and the surface density of each annulus has been computed by calculating the total H I mass of the annulus divided by its surface area. The figure shows the profiles for both the **L08** (blue) and **GK11** (red) method of computing the molecular fraction.

Although some variability is present between the different profiles, a general trend can be identified. Starting from the centre of the profile, the H I surface density increases up to a point where it reaches a plateau of approximately constant surface density. After this plateau, which in some cases (e.g. Au 2, Au 16, Au 20) can extend up to 10 kpc, Σ_{HI} drops quite rapidly, and very lit-

tle H I is left past R_{HI} . The density plateau is not always present. Some profiles (e.g. Au 6, Au 12, Au 13, Au 14, Au 21, Au 26) instead show an increase of Σ_{HI} up to a maximum value after which the profiles immediately decline. Other profiles (e.g. Au 11, Au 30) show a monotonic decrease of the H I surface density at all radii, but we note that this could be due to interactions with close, massive companions that they are currently experiencing.

It is also interesting to compare the difference in the H I radial profiles due to the two different methods that we have used to take into account the contribution of the molecular gas to the total neutral H density. In general, it can be seen that the two methods agree very well at large radii (i.e. $R \sim R_{\text{HI}}$), where the contribution of molecular hydrogen to the total budget is negligible. The agreement still remains remarkable at intermediate radii, where the surface density plateau or the maximum value of Σ_{HI} are reached, but close to the centre, the **GK11** method generally results in more depressed profiles (but see Au 11, Au 13, Au 26 for the opposite trend). In Section 4.5, we discuss in more detail what these differences imply for the global properties (such as the total H I mass) and scaling relations of the simulated gas discs.

In Fig. 7 we show the median H I radial profiles for the 30 Auriga haloes computed with the **L08** (blue symbols with error bars) and the **GK11** (red symbols with error bars) prescriptions for estimating the molecular hydrogen fraction. The median values have been obtained by interpolating the profiles presented in Figs. 5 and 6 as a function of the galactocentric distance (normalized to R_{HI}) onto a uniformly spaced radial grid of width $0.1 \times R/R_{\text{HI}}$. Error bars indicate the region between the 16-th and 84-th percentiles of each radial bin of the simulated H I profiles. The simulation results are compared with the median profile (obtained with the same pro-

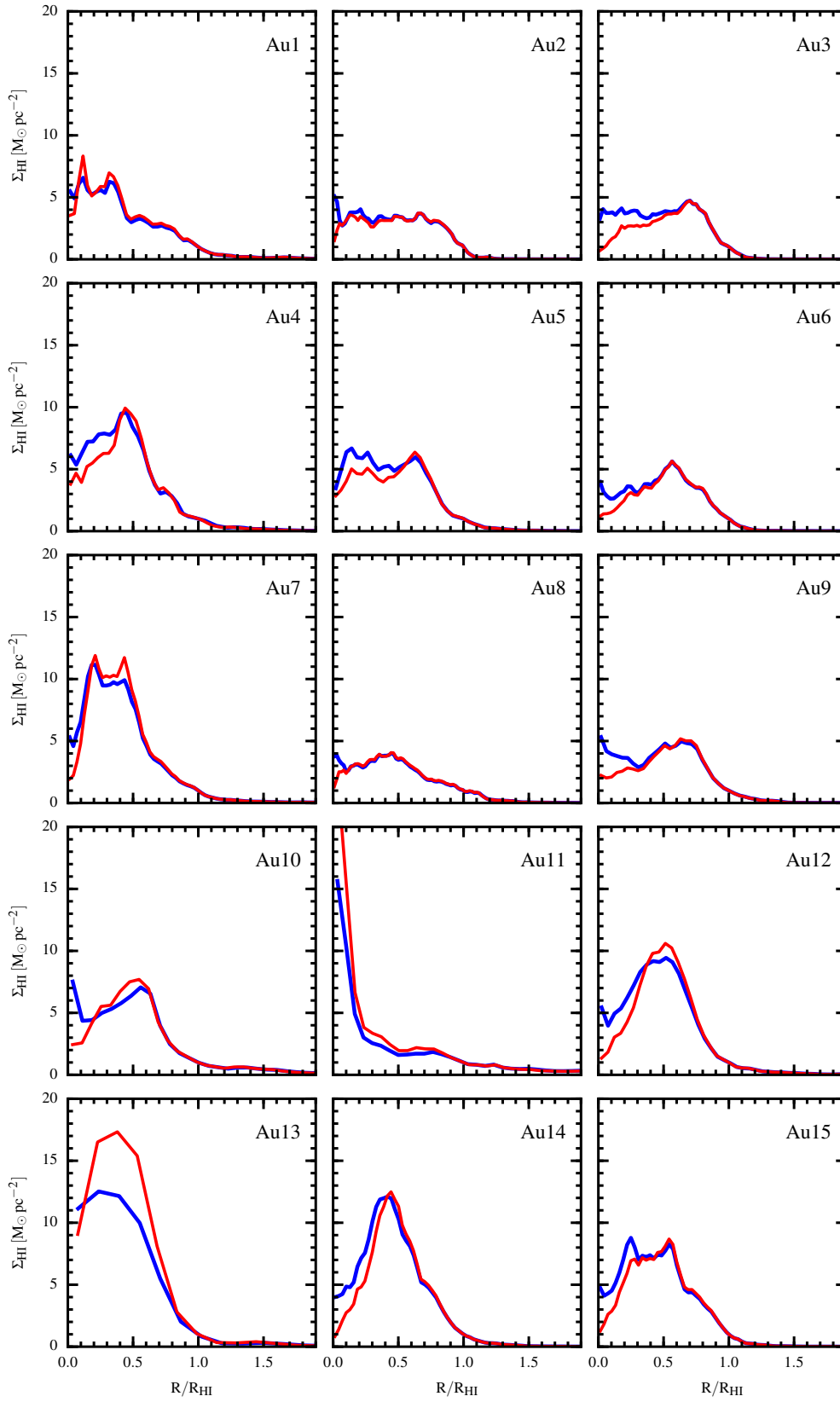


Figure 5. H I surface density profiles as a function of the galactocentric radius (in units of the H I radius of each galaxy, see Table 1) for haloes Au 1 to Au 15. The blue and red lines indicate the profiles obtained using the prescription from L08 or GK11 for removing molecular gas, respectively.

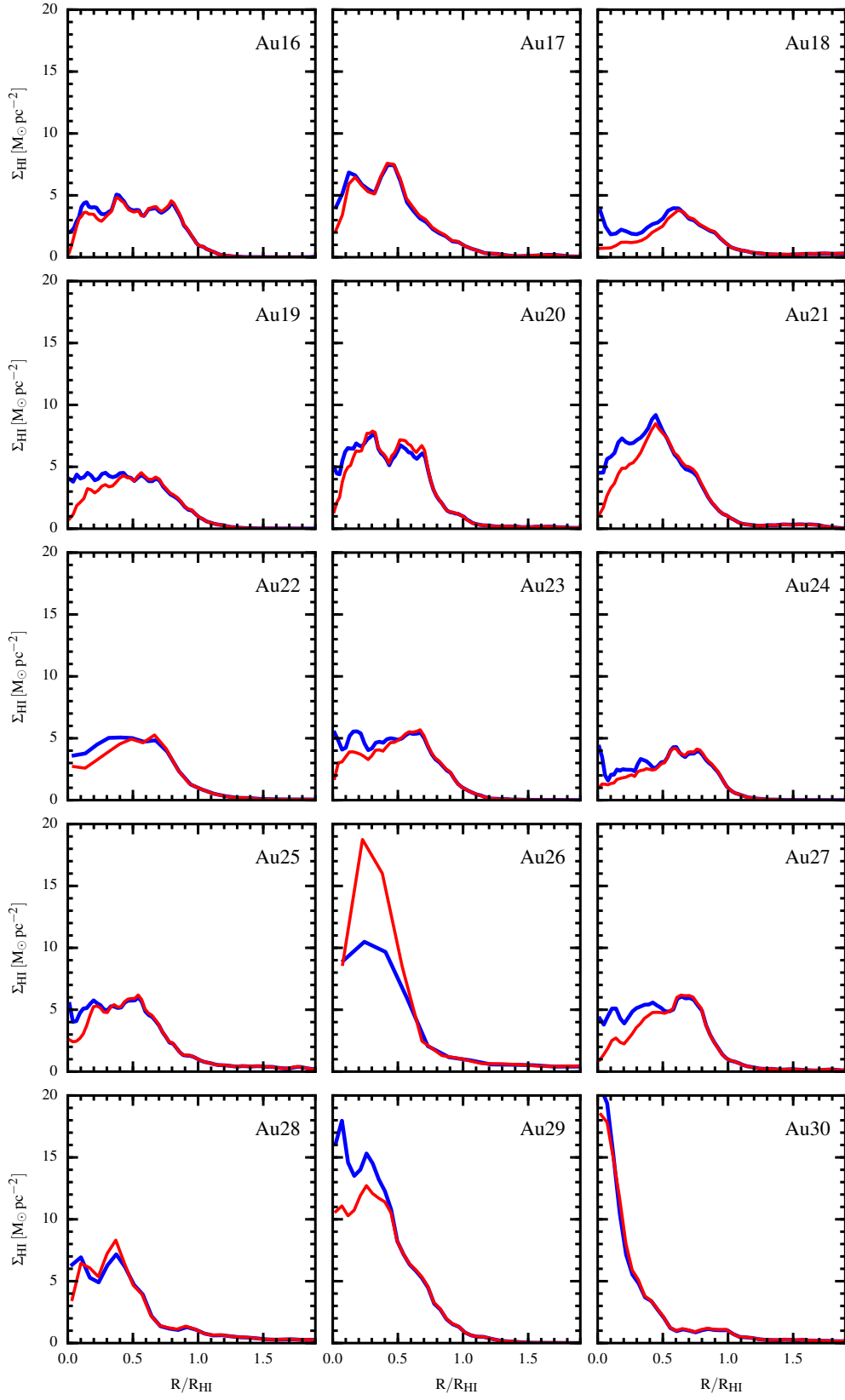


Figure 6. As in Fig. 5, but for haloes Au 16 to Au 30.

Run	R_{HI}^{L} [kpc]	M_{HI}^{L} [$10^9 M_{\odot}$]	$\Sigma_{\text{HI}}^{\text{L}}$ [$M_{\odot} \text{ pc}^{-2}$]	h_{HI}^{L} [kpc]	$R_{\text{HI}}^{\text{GK}}$ [kpc]	$M_{\text{HI}}^{\text{GK}}$ [$10^9 M_{\odot}$]	$\Sigma_{\text{HI}}^{\text{GK}}$ [$M_{\odot} \text{ pc}^{-2}$]	$h_{\text{HI}}^{\text{GK}}$ [kpc]
Fiducial resolution (level 4)								
Au 1	29.7	8.1	2.9	1.9	29.9	8.7	3.1	2.4
Au 2	49.9	22.3	2.9	1.7	50.0	22.0	2.8	1.8
Au 3	42.0	18.3	3.3	1.7	42.2	17.0	3.0	2.3
Au 4	22.9	7.4	4.5	2.7	23.5	7.6	4.4	4.9
Au 5	24.5	7.3	3.8	1.9	24.7	7.0	3.7	2.9
Au 6	38.0	15.0	3.3	1.6	38.2	14.8	3.2	1.9
Au 7	35.4	18.0	4.6	4.3	35.5	19.1	4.8	5.8
Au 8	54.8	22.2	2.3	1.8	55.1	22.9	2.4	1.9
Au 9	24.5	6.4	3.4	1.3	24.7	6.3	3.3	1.8
Au 10	13.3	2.2	3.9	1.7	13.6	2.4	4.1	4.1
Au 11	15.3	1.4	1.9	3.5	15.1	1.7	2.3	4.5
Au 12	19.9	6.7	5.3	2.2	20.2	7.0	5.5	4.8
Au 13	7.1	0.8	5.0	1.7	7.3	1.1	6.8	2.5
Au 14	34.7	21.5	5.7	4.5	34.8	21.2	5.6	6.2
Au 15	34.0	17.2	4.7	3.1	34.1	17.1	4.7	4.7
Au 16	52.2	29.3	3.4	2.0	52.3	29.2	3.4	2.4
Au 17	20.4	4.5	3.5	2.3	20.5	4.7	3.5	3.4
Au 18	25.0	5.0	2.5	1.2	25.1	4.6	2.3	1.5
Au 19	36.2	13.0	3.2	1.5	36.3	12.7	3.1	1.9
Au 20	46.9	29.4	4.3	3.7	47.1	30.8	4.4	4.3
Au 21	34.8	17.8	4.7	2.7	34.9	17.0	4.4	4.5
Au 22	11.2	1.4	3.6	1.0	11.3	1.4	3.4	1.5
Au 23	34.8	14.5	3.8	1.7	35.0	14.2	3.7	2.1
Au 24	43.9	18.3	3.0	1.3	44.0	18.0	2.9	1.7
Au 25	37.8	15.6	3.5	2.5	37.9	15.6	3.5	3.0
Au 26	5.6	0.5	4.9	3.9	5.9	0.7	6.7	10.4
Au 27	32.0	13.7	4.3	1.9	32.2	13.0	4.0	2.7
Au 28	14.7	2.0	2.9	4.9	14.9	2.1	3.0	9.2
Au 29	22.6	8.4	5.2	4.5	22.7	7.9	4.9	5.3
Au 30	18.3	2.6	2.4	2.7	19.1	2.8	2.4	3.8
Low resolution (level 5)								
Au 16	61.1	39.2	3.3	3.4	61.4	40.8	3.5	3.4
Au 24	30.6	13.2	4.5	2.0	30.7	13.5	4.6	2.3
High resolution (level 3)								
Au 16	57.9	27.3	2.6	1.6	58.2	26.6	2.5	2.3
Au 24	43.1	17.8	3.0	1.8	43.3	17.0	2.9	2.4

Table 1. Properties of HI discs in the Auriga simulations. The columns list (from left to right): simulation name; HI radius, HI mass, average HI surface density and HI scale height (L08 method); HI radius, HI mass, average HI surface density and HI scale height (GK11 method).

cedure) of the Bluedisk sample (Wang et al. 2014, grey solid line). The shaded grey area indicates again the region between the 16-th and 84-th percentiles in each radial bin of the observed Bluedisk radial profiles.

A comparison between the median simulated profiles reveals that they are very similar at all radii, and that they start to differ only in the innermost regions where the GK11 profile starts to show a decrease in the HI surface density, which is however less marked than the one observed in the individual profiles. Compared to the Bluedisk sample, both the L08 and the GK11 median profiles are largely consistent with observations although some discrepancies are present. In particular, the simulated profiles overpredict the values of the HI surface density in the radial range $0.4 \lesssim R/R_{\text{HI}} \lesssim 0.8$.

It is also instructive to compare our results with those found in the EAGLE simulations (B16), in which the more local and violent nature of the stellar feedback results in \sim kpc-scale holes in the

(neutral) gas distribution. This, in turn, impacts the HI radial profiles of the EAGLE galaxies, with the result that in the central parts the median HI profile is underestimated with respect to the observations. The Auriga galaxies, thanks to a more distributed stellar feedback and an ISM model adopting an effective equation of state (see Springel & Hernquist 2003), do not suffer from this problem. In fact, they tend to overpredict the HI content at intermediate radii. Moreover, the discrepancies in the radial profiles (but also other HI related quantities, see next sections) due to a different choice of the prescription used to model the contribution of molecular hydrogen are negligible in the Auriga case (except for a depletion of HI in the innermost regions), while in EAGLE they are significantly larger. Indeed, even considering a simulated galaxy sample in which big HI holes are not present, the GK11 method systematically underpredicts the HI surface density in the central region of the EAGLE galaxies, while eq. (3) – with a slightly different choice of param-

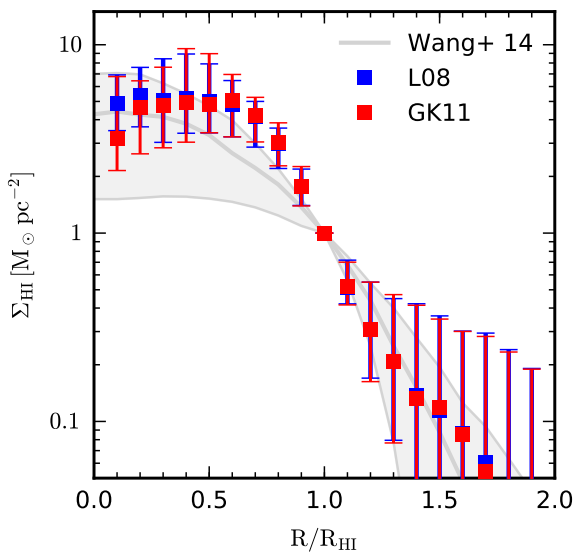


Figure 7. Median H I profiles for the 30 Auriga haloes derived with the L08 (blue symbols) and GK11 (red symbols) prescriptions for the treatment of molecular hydrogen. For comparison, the median H I profile for the Bluedisk sample (Wang et al. 2014, grey lines) is shown. Error bars and the shaded grey region indicate the area between the 16-th and 84-th percentiles of each radial bin (of size $0.1 R_{\text{HI}}$) of the three distributions.

eters than in the present work (see Blitz & Rosolowsky 2006) – reproduces the observations fairly well.

4.3 H I vertical distribution

We now focus on the vertical structure of our simulated H I discs. As it is apparent from the edge-on column density maps presented in Sec. 4.1, the vertical extent of the H I layer varies for each object. Here we want to analyse this variation in a more quantitative way and relate it to the internal properties of the central galaxy, in particular to its star formation rate. There are, of course, processes external to the galaxy that will also affect the vertical H I distribution, such as mergers (see e.g. the cases of Au 11 and Au 30) or close interactions with satellites (e.g. Au 18), which however we do not discuss in the present work (but see Gómez et al. 2016a,b, for an analysis of the impact of these effects on the vertical motion of gas and stars within galactic discs).

It is worth recalling that in our galaxy formation physics model, galactic outflows are powered by supernova explosions. The energy of these outflows is related to the global star formation rate of the galaxy. It is thus natural to expect a relation between this property and the structural properties of the H I disc, such as for instance the vertical scale height. Figure 8 presents the corresponding correlation obtained with the two different methods we used to compute the molecular hydrogen mass fraction (blue symbols for the L08 and red symbols for the GK11 prescription, respectively) together with their best-fitting relations (dashed lines of the same colours). The best-fitting parameters are given in the legend. To select the actively star forming region of the galaxy, we consider only the region of the disc within the optical radius of the galaxy R_{opt} , computed as the galactocentric radius at which the B-band surface brightness profile reaches $25 \text{ mag arcsec}^{-2}$. We then estimate the total star formation rate of the galaxy and the H I mass in a cylinder of radius R_{opt} , extending $\pm 30 \text{ kpc}$ outside the disc plane. Finally,

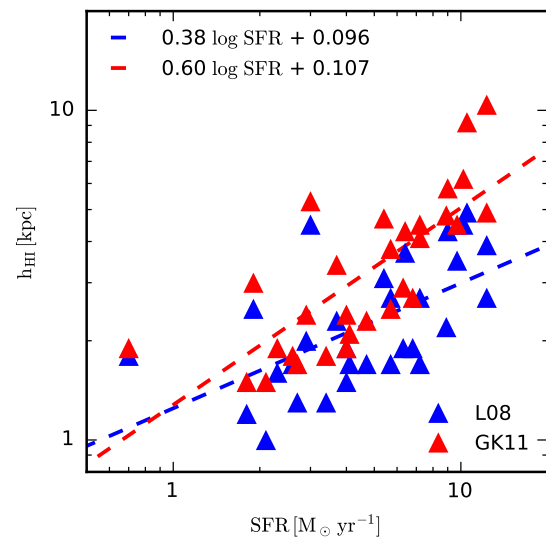


Figure 8. H I vertical thickness (defined as the height containing 75% of the H I mass) as a function of the SFR within the galaxy B-band optical radii for the 30 Auriga haloes derived with the L08 (blue symbols) and GK11 (red symbols) prescriptions for the treatment of molecular hydrogen. Dashed lines represent the best-fitting relations in the two cases, with parameters indicated in the legend.

we define the H I scale height h_{HI} as the height containing 75% of the H I mass determined in the step above. The inferred values of h_{HI} for both the L08 and GK11 methods are presented in Table 1.

Figure 8 shows a correlation between the H I scale height and the SFR of the central galaxy, with more actively star forming galaxies having larger values of h_{HI} . Overall, this relationship between the star forming properties of the galaxy and the scale height of its H I layer is consistent with the theoretical picture that galactic fountain flows generated by stellar feedback can push a significant fraction of the H I mass outside the galaxy mid-plane (see e.g. Fraternali & Binney 2006, 2008; Marasco & Fraternali 2011). This is also in agreement with the so-called upside-down disc formation scenario in which a declining SFR leads to a gas disc getting thinner with time (see Grand et al. 2016b, for a detailed analysis of this in the Auriga sample). The degree of scatter around the best-fitting relation is significant, supporting the idea that also external processes contribute to building of the H I layers. The correlation is present regardless of the technique used to estimate the molecular gas fractions in the simulations, but it is actually steeper – and the associated H I scale heights are larger – for the GK11 method.

4.4 Differences in the global H I properties

From the profiles computed in Sec. 4.2 it is possible to derive the total H I mass of the galaxy as the mass of all the gas cells within R_{HI} . We report these values in Table 1 for all the 30 objects we have simulated³, together with their H I radii and the average H I surface density within R_{HI} , for the two different methods we have used to remove the contribution of molecular hydrogen.

Figures 9 and 10 illustrate the differences between the recovered H I diameters and H I masses, respectively, for both the L08 and

³ Data are also available in electronic format at <http://auriga.h-its.org/data.html>

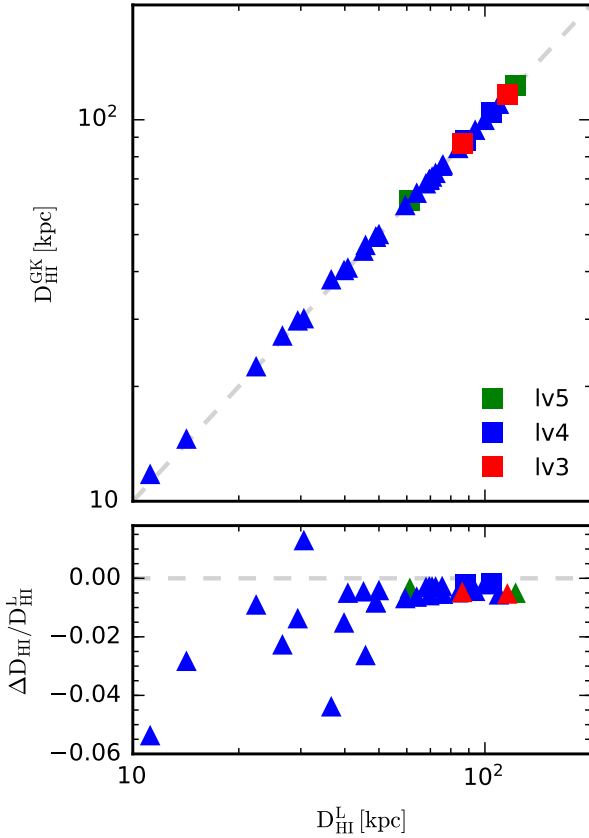


Figure 9. HI diameter mass obtained by using the L08 and the GK11 prescription to account for the molecular gas for the 30 Auriga haloes. Top panel: comparison of the HI diameters obtained in the two cases. Bottom panel: fractional variation with respect to the L08 HI diameter as a function of the L08 HI diameter. Dashed lines in both panels show the 1:1 correspondence.

GK11 methods to account for molecular hydrogen. The top panels of both figures present a direct comparison between the two methods, while the bottom panels show their fractional variation with respect to the L08 value. Different colours show simulations at different resolution levels (see Sec. 4.7 for more details), while the dashed lines indicate the 1:1 correspondence.

Let us first focus on $D_{\text{HI}} \equiv 2R_{\text{HI}}$. We have already mentioned in Sec. 4.2 that at large radii ($R \sim R_{\text{HI}}$) the method used to compute the molecular fraction has a negligible impact on the results. Therefore, it is not surprising that the HI diameters estimated with the two methods agree so well. Basically, all the simulated points lie very close to the 1:1 expectation. The fractional difference between the two D_{HI} values is of the order of a few per cent. The general outcome is that the GK11 method tends to recover slightly larger values for the HI diameter. There is no obvious trend of the fractional differences as a function of the HI size of the simulated objects, although it seems that they are more pronounced at smaller D_{HI} .

The same conclusions can be reached for the HI masses, although here the differences are larger (of the order of 10% and reaching up to 40% for small masses). However, in this case the fractional differences between the two masses are spread approximately evenly around the 1:1 value. This can be explained by the

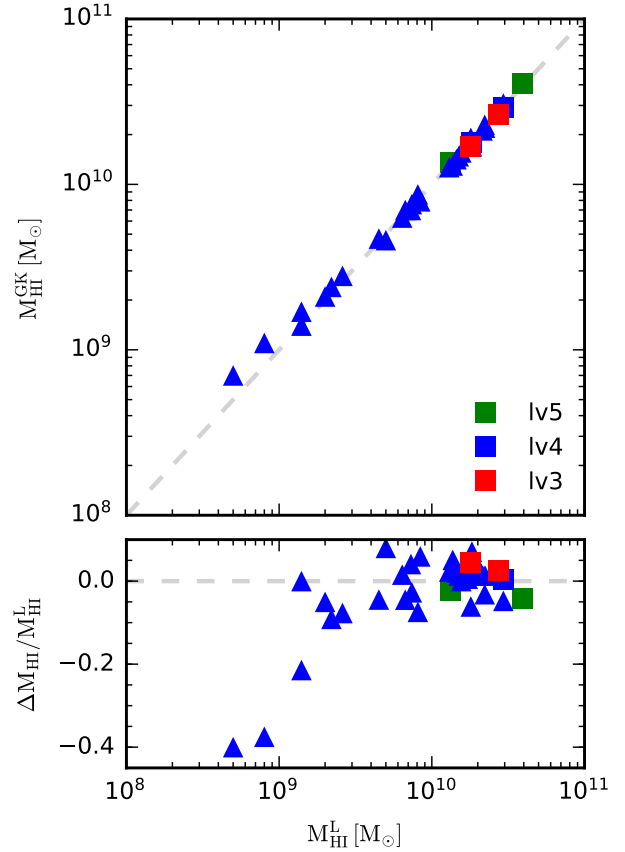


Figure 10. As in Fig. 9, but for the inferred HI mass of the Auriga sample.

fact that the HI diameters recovered by the GK11 method are consistently larger than their L08 counterparts, which compensates for the smaller HI column densities found in the inner regions of the disc for the GK11 method. Again, there is no obvious trend in the fractional differences as a function of the HI mass, although the differences become more distinct at low M_{HI} .

4.5 The mass-diameter relation

An important scaling relation in HI observations of nearby disc galaxies is the one linking the total HI mass of the galaxy to the size of the HI disc, the so-called mass diameter relation (Broeils & Rhee 1997; Verheijen & Sancisi 2001; Swaters et al. 2002; Noordermeer et al. 2005; Martinsson et al. 2016). Figure 11 shows this relation for our simulated sample of galaxies for the L08 (blue symbols) and the GK11 (red symbols) methods to account for the molecular hydrogen. The lines on the left-hand panel show the best fit to this relation of the form

$$\log \left(\frac{M_{\text{HI}}}{M_{\odot}} \right) = \alpha \log \left(\frac{D_{\text{HI}}}{\text{kpc}} \right) + \beta, \quad (8)$$

with the best-fitting parameters given in the legend. The lines on the right-hand panel indicate the best-fitting relations derived from observations of nearby galaxies (Verheijen & Sancisi 2001; Martinsson et al. 2016; Ponomareva et al. 2016). We also show, as empty symbols, observational results taken from the SPARC galaxy sample (Lelli et al. 2016) to give an indication of the observed scatter in the relation. Our simulated galaxies reproduce the same gen-

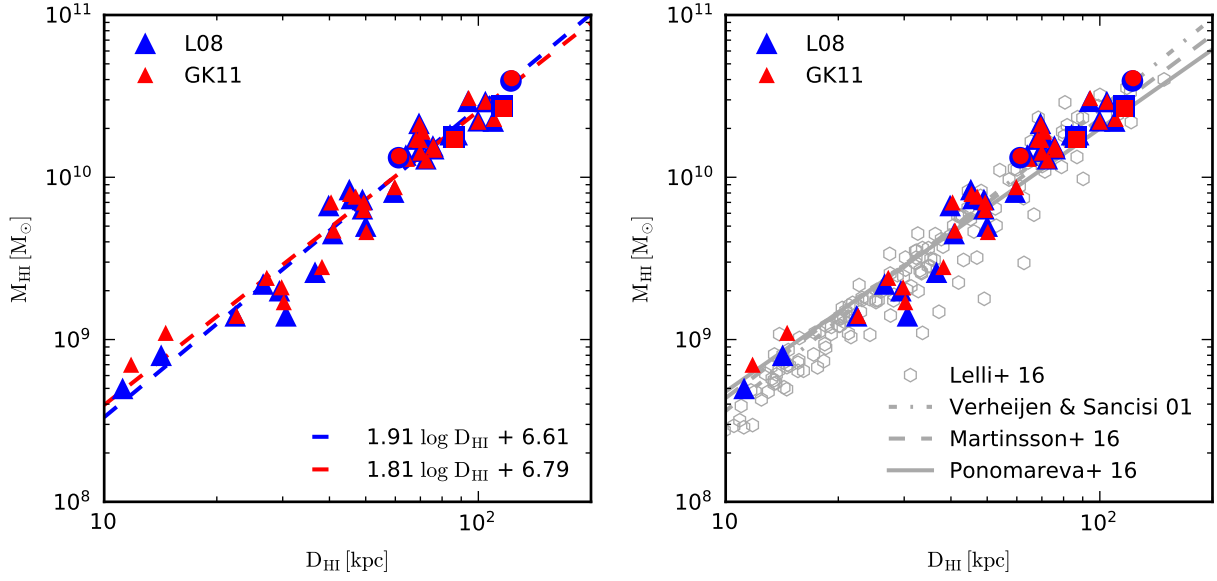


Figure 11. The H I mass diameter relation for the Auriga galaxies. Blue symbols show the results obtained with the empirical relation from L08 to account for molecular gas, while red symbols show the outcome of the prescription described in GK11. Lines in the left panel show the best-fitting relation inferred from the two samples, while lines and empty symbols in the right panel compare the Auriga findings to observations of nearby galaxy as shown in the legend. Triangles present the results obtained at the standard (level 4) resolution, while circles and squares show haloes Au 16 and Au 24 at resolution levels 5 and 3, respectively.

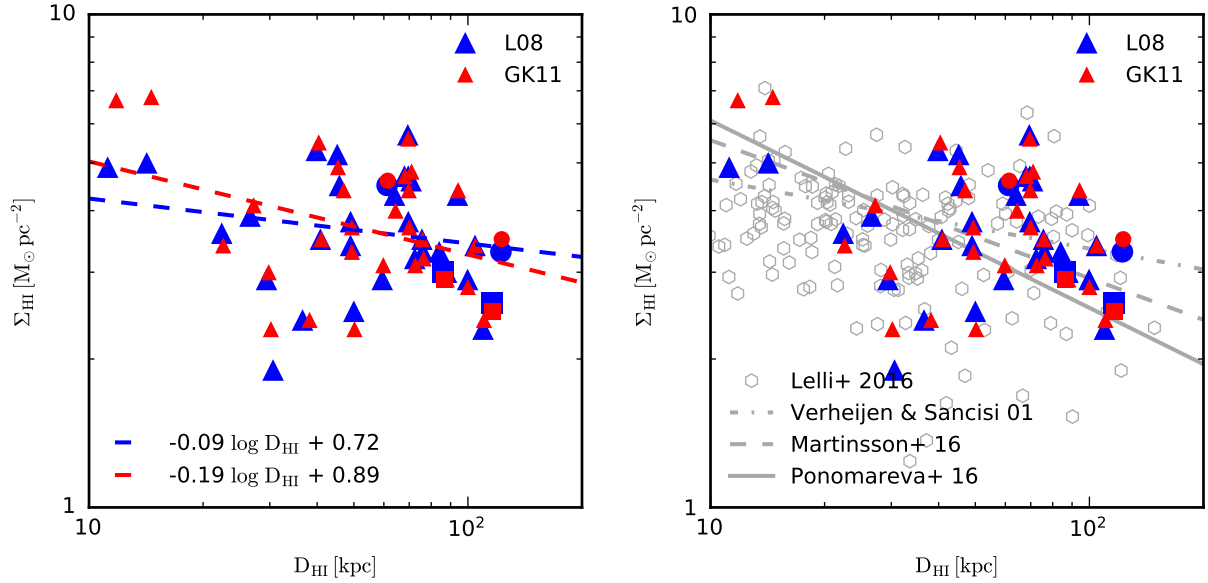


Figure 12. As in Fig. 11, but showing the mean H I column density within D_{HI} as a function of the H I diameter. Lines in the left panel show the mean H I column density trends derived from the relations presented in Fig. 11. Similarly, lines and empty symbols in the right panel compare the Auriga findings to observations of nearby galaxies as shown in the legend.

eral trend seen in observations, in which a larger H I size corresponds to a higher H I mass, and they agree with the observed scaling relation(s) (right panel) very well. The best-fitting relations inferred from the simulated L08 and GK11 samples are also in good agreement with one another, the L08 relation being slightly steeper. Reassuringly, this degree of variability in the slope of the mass-

diameter relation is also present in the observationally-derived relations.

Our results on the mass-diameter relation are in agreement with the findings by B16, who report that EAGLE galaxies are consistent with the observational constraints. More precisely, B16 compare their simulated H I discs to the Broeils & Rhee (1997) best-fitting relation which is not shown in Fig. 11 but is equivalent (its

slightly higher slope is compensated by a lower zero-point) to the ones considered in our analysis. Therefore, we conclude that, unlike the HI surface density radial profiles, the mass-diameter scaling relation is a very robust outcome of simulations, even for very different treatments of the star-forming gas and stellar feedback. However, contrary to the B16 analysis, we do not observe a dramatic change in slope of the mass-diameter relation in the GK11 case.

Observations have also shown that the average HI surface density within R_{HI} is an approximately constant or slowly declining function of the HI diameter. In Fig. 12 we present the relation between these two quantities. The meaning of the symbols and of the best-fitting line is the same as in Fig. 11. However, we would like to point out that in this case we did not perform a fit of our simulated data points, but rather we have taken the best-fitting parameters for the mass-diameter relation and converted them in terms of the (average) surface density as

$$\log \left(\frac{\Sigma_{\text{HI}}}{\text{M}_{\odot} \text{pc}^{-2}} \right) = (\alpha - 2) \log \left(\frac{D_{\text{HI}}}{\text{kpc}} \right) + \beta - 5.9. \quad (9)$$

The same procedure has also been adopted for the observed mass-diameter relations. Although there is considerably more scatter than in the previous case, also for this scaling relation our simulated objects recover well the observed trend of a slowly declining HI surface density with increasing HI size. Again, the amount of scatter in the relationship and the variability of the best fitting parameters are consistent with the observational findings.

4.6 Gas fractions

In Fig. 13 we present the HI gas fractions [$f_{\text{gas}} \equiv M_{\text{HI}}/(M_{\star} + M_{\text{HI}})$] as a function of the stellar mass for the Auriga sample. Stellar masses are computed within 10% of the virial radius of each object (see also Marinacci et al. 2014a; Grand et al. 2016a), and the HI gas masses are those reported in Table 1. Different colours indicate the two different methods to compute the contribution of molecular hydrogen, as indicated in the legend. The simulation results are compared to both the GASS (Catinella et al. 2013) and Bluedisk (Wang et al. 2013) samples. The Bluedisk sample is further split between gas-rich galaxies (full symbols) and a control sample (empty symbols), as in Wang et al. (2013).

Although the simulated range in stellar masses is somewhat reduced compared to observations – remember that the Auriga haloes were selected to be a match for the Milky Way – the Auriga set shows a declining HI gas fraction for increasing stellar mass as in the observations. The decline in the gas fraction is comparable to the observations, with an abrupt decrease at $M_{\star} \sim 6 \times 10^{10} \text{M}_{\odot}$ where f_{gas} drops from 10% to about 1%. These trends are robust with respect to the model used to compute the molecular hydrogen fraction with almost no difference in the recovered gas fractions, except at the very high end of the stellar mass spectrum where however the difference is within a factor of 2.

The gas fractions of the Auriga set are consistent with the observations, albeit the simulated galaxies are systematically more gas-rich than the average for their stellar mass. If one considers the GASS sample, it can be readily seen that the Auriga set is at the upper envelope of the observed galaxies. If, instead, the Bluedisk sample is considered, the simulated galaxies follow more closely the trend of the gas-rich sample (which notably is composed of galaxies with HI mass fractions 0.6 dex higher than the median relation found in Catinella et al. 2010) than the one of the control sample comprised of more “average” galaxies. This occurs for stellar

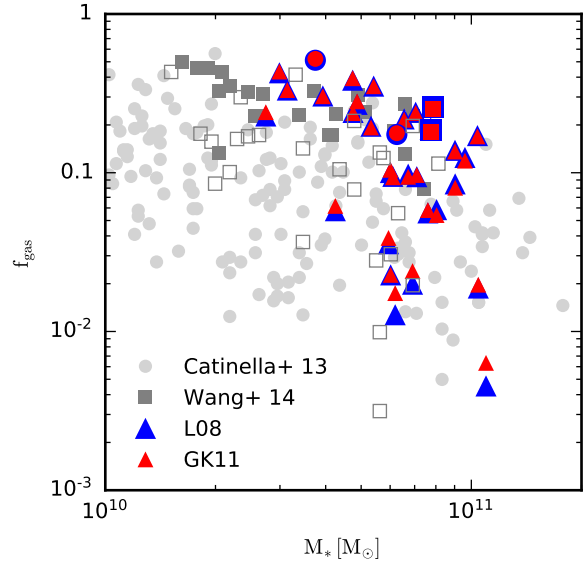


Figure 13. HI gas fraction as a function of the stellar mass for the Auriga sample. Stellar masses are computed within 10% of the virial radius of each object, while HI masses are those listed in Table 1. Results obtained through the empirical relation in L08 to account for molecular gas are shown with red symbols, while those obtained by applying the GK11 prescription are represented by blue symbols. Triangles give the results obtained at the standard (level 4) resolution, while circles and squares show haloes Au 16 and Au 24 at resolution levels 5 and 3, respectively. Grey symbols indicate observational findings from the GASS (Catinella et al. 2013) and the Bluedisk (Wang et al. 2014) surveys, as indicated in the legend. For the combined datasets, only 195 out of 300 galaxies which were significantly detected in HI are shown.

masses below the value $M_{\star} \sim 6 \times 10^{10} \text{M}_{\odot}$. As already discussed above, for stellar masses larger than this value, f_{gas} drops quite abruptly to the 1% level, a value fully consistent with the observations. The fact that the Auriga galaxies are generally more gas-rich than the observations should not be surprising given the results already discussed in Sections 4.2 and 4.5, in which we showed that our simulations overpredict the average surface density of the HI discs and preferentially populate the high-mass, large-size part of the mass-diameter relation. Given that the stellar masses recovered by the Auriga project are consistent with abundance matching predictions (Grand et al. 2016a), we attribute this higher HI content to the fact that the method presented in Sec. 3.1 tends to overestimate the neutral gas fraction of the star-forming gas since no corrections for photoionisation (originating from the cosmic UV background and the local stellar radiation field) are applied.

4.7 Resolution dependence

Up to now we have used our fiducial resolution level to analyse the HI properties of the Auriga galaxies. A few selected galaxies in the Auriga set have been re-simulated also at different mass and spatial resolution levels. These additional simulations have been performed with the same galaxy formation physics model as the fiducial runs; only the number of resolution elements in the high-resolution region (and consequently the force resolution of the simulations) has been modified. In this section, we are interested in checking how robust the results of our HI analysis are with respect to a change in the resolution of the runs.

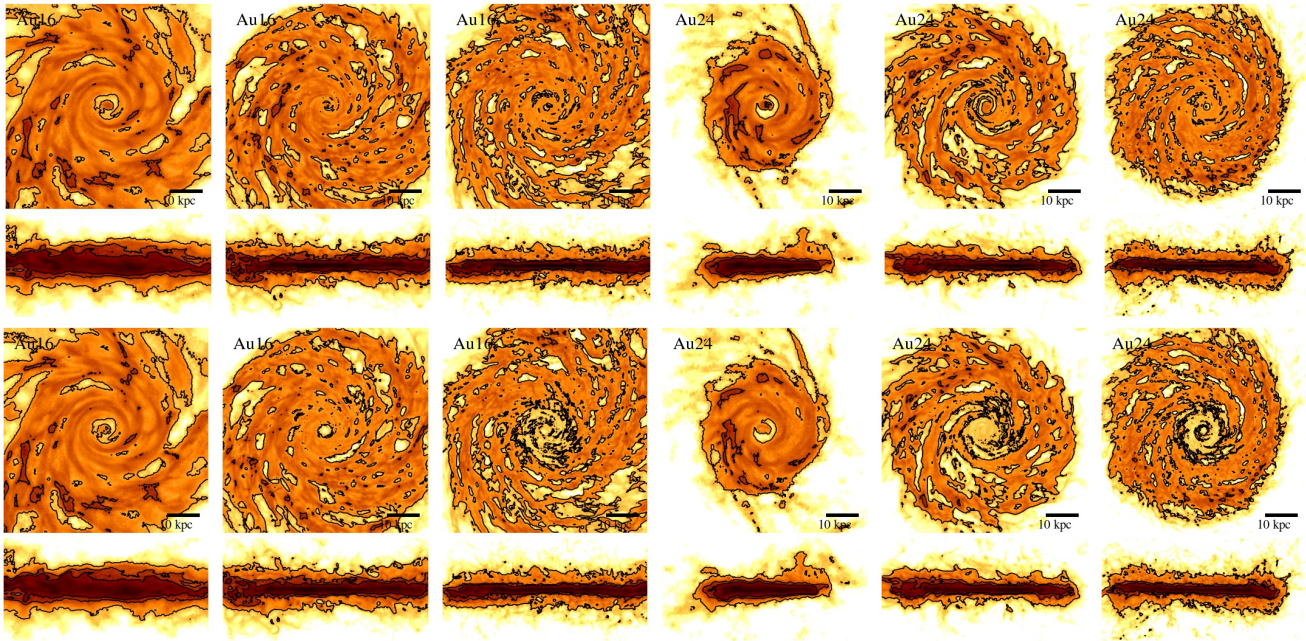


Figure 14. Resolution study for the H I column density maps of haloes Au 16 and Au 24. From left to right and for each halo, the resolution level varies from the least resolved to the most resolved. The top row shows the maps obtained using the prescription from L08 for removing molecular gas, while the H I maps in the bottom row adopt the GK11 approach. The size of the projected region is 90 kpc on a side for face-on projections and 90×45 kpc for the edge-on ones.

We first introduce a naming convention for easy reference to runs differing only in numerical resolution. Following the nomenclature adopted in the Aquarius project (Springel et al. 2008), we identify each resolution level with a numeral. A difference of one resolution level means a finer (or coarser) mass resolution by a factor of 8, thus implying a spatial resolution (i.e. a softening length) which can be finer (or coarser) by a factor of 2. The lower the numeral identifying the resolution level, the finer the effective (mass and spatial) resolution. In what follows, we are going to analyse three different resolution levels for the haloes Au 16 and Au 24: our fiducial runs at resolution level 4, and finer (level 3) and coarser (level 5) realizations.

Figure 14 presents H I face-on and edge-on density projections (in a way akin to Figs. 2 to 4) for the haloes Au 16 and Au 24. The top row in each figure shows the H I surface density obtained with the L08 prescription to compute the contribution of molecular hydrogen, while in the bottom row the GK11 model has been used. The resolution increases for each halo from left to right such that each column in the figure represents H I density projections of either halo Au 16 or Au 24 at the same resolution level but obtained with different treatments for molecular hydrogen.

From the figure it can be seen that the main morphological traits of the H I discs are present for both haloes at all 3 different resolution levels. Not surprisingly, higher resolution brings out finer details in the gas distribution. In particular, in the edge-on projections it is apparent that the thin component of the H I disc is better defined at the highest resolution level, while the vertical gas distribution puffs up considerably at the lowest resolution. The central depletion in the H I content for the GK11 method is barely noticeable at the lowest resolution level for both haloes, but it is increasingly more visible at higher resolution – note how the size of the central H I ‘hole’ increases in size for the Au 16 halo. The most striking difference, however, concerns the radial extent of the H I disc in the halo Au 24. Indeed, at resolution level 5 the H I disc is

significantly less extended than in the two higher resolution levels, where the size of the H I disc appears similar. Halo Au 16 is not affected by this discrepancy, and the variation of the disc size across the different resolution levels is smaller.

Figure 15 presents H I surface density profiles as a function of the galactocentric radius (normalized to R_{HI}) for haloes Au 16 (top) and Au 24 (bottom). Line colours show the results obtained with the L08 (blue) and GK11 (red) prescriptions to compute the molecular hydrogen mass fraction, while their line-style identifies the resolution level as indicated in the legend. Light grey lines are the H I surface density profiles of the Bluedisk survey and are shown for comparison.

The H I radial profiles show the general trends already discussed in Sec. 4.2, that is an increasing H I surface density profile in the innermost regions which reaches a maximum value or a plateau and then quickly drops at $R \simeq 0.85 \times R_{\text{HI}}$, leaving little gas past the H I radius of the galaxy. The H I surface density profiles are overall very similar across the resolution levels. Only level 5 presents marked differences with respect to the two finer resolution levels, in particular for halo Au 24. In general, the profiles for level 4 and level 3 track one another closely, regardless of the prescription adopted to estimate the molecular gas fraction, although for halo Au 16 the level 4 profile predicts an H I column density about a factor of 2 larger than the corresponding level 3 profile at $R \sim 0.8 \times R_{\text{HI}}$. A comparison of the simulated profiles with those obtained in the Bluedisk survey shows that the profiles of the Auriga galaxies are consistent with the observed ones, although occasionally (for example for halo Au 16 at level 4 and halo Au 24 at level 5) there is an excess of H I at $R \simeq 0.8 \times R_{\text{HI}}$.

Starting from the radial H I density profiles it is possible to derive the structural properties of the H I discs (sizes, total masses and average densities) at the additional resolution levels in the same way as done for the fiducial resolution. We report these values in Table 1 under separate headings for the different resolution levels.

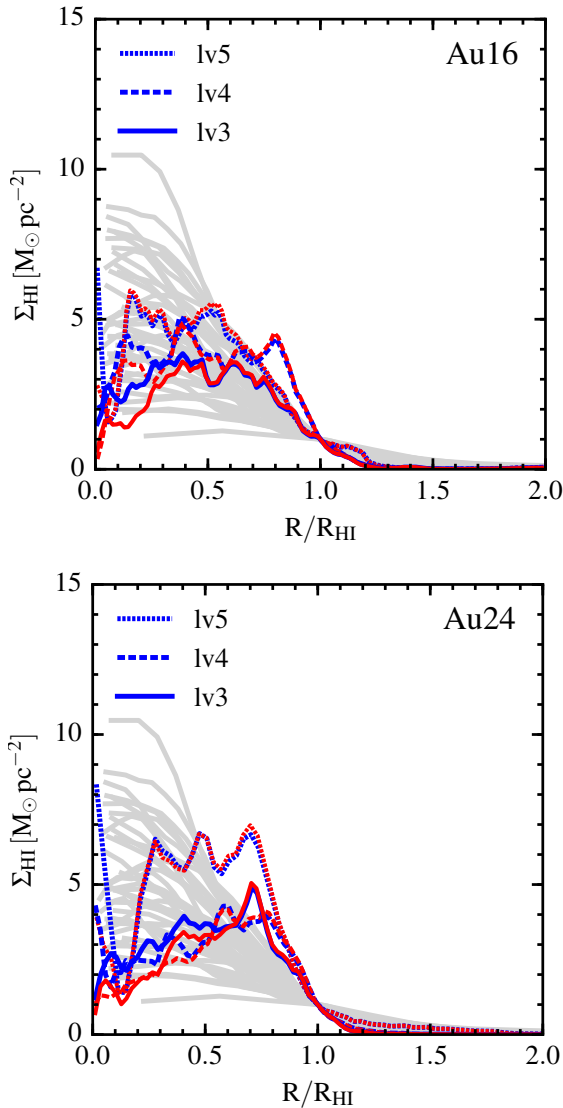


Figure 15. Resolution study for the HI surface density profiles for haloes Au 16 and Au 24. The blue and red lines indicate the profiles obtained using the prescription from L08 or GK11 for removing molecular gas, respectively. The line style indicates the resolution level, as given in the legend. Light grey lines display the HI radial profiles of the Bluedisk survey (Wang et al. 2014).

Clearly, it is possible to investigate several scaling relation between these quantities, as already done in Sections 4.4 to 4.6, allowing us to check the robustness of our findings with respect to resolution changes. To this end, we added the relevant data points for haloes Au 16 and Au 24 at resolution levels 5 and 3 to the plots presented above, either in different colours (Figs. 9 and 10) or with different symbols (circles for level 5 and squares for level 3, see Figs. 11 to 13). Although differences between the sizes, masses and average densities exist across the three resolution levels, the individual data points follow the general pattern determined by the full set of 30 simulations at resolution level 4, meaning that each individual galaxy follows the general scaling relations derived for the full sample.

From these considerations we can conclude that our findings are robust with respect to changes in mass resolution (over a fac-

tor of 64) and this holds regardless of the prescription adopted to estimate the contribution of the molecular gas to the total neutral hydrogen density. While some discrepancies do exist between the different resolution levels, they tend to decrease with increasing resolution. In particular, our fiducial resolution level seems to be adequate to model the HI content of Milky Way-like systems with sufficient accuracy.

5 SUMMARY AND CONCLUSIONS

In this paper we have analysed the properties of the HI distribution in the Auriga simulations, a set of cosmological magnetohydrodynamic simulations run with the moving-mesh code AREPO that investigate the formation and evolution of disc galaxies similar to our own Milky Way. We have modelled the HI gas by computing the neutral hydrogen fraction separately for low-density and star-forming gas, which, in the star formation module currently implemented in our simulations, is described by an effective equation of state and thus requires a special treatment to calculate its neutral fraction in a meaningful way. To estimate the contribution of molecular gas to the total neutral hydrogen mass we have used two different prescriptions – motivated by observational and theoretical studies – and compared their outcomes. Our main results can be summarized as follows.

(i) The vast majority of the simulated systems feature an extended (i.e. more extended than the associated stellar distribution) HI disc which in some cases may reach a radial extent of ~ 60 kpc. A few objects (i.e. Au 11 and Au 30) present disturbed morphologies as a consequence of late-time galaxy interactions.

(ii) The vertical extent of the HI distribution varies on a system by system basis. The amount of HI gas outside the disc plane correlates with the amount of star formation occurring in the (stellar) disc, in agreement with a scenario where most of the extra-planar HI gas results from a fountain-like gas flow (Fraternali & Binney 2006, 2008; Marasco & Fraternali 2011).

(iii) The (face-on) radial profiles of the HI surface density show a common pattern in which the HI surface density stays approximately constant and then exponentially drops at $\sim R_{\text{HI}}$, in good agreement with observations. Contrary to previous theoretical studies (B16), our simulated galaxies do not show a deficiency of HI in the central region, but rather overpredict the HI contents at galactocentric radii $R \simeq 0.5 R_{\text{HI}}$.

(iv) Our simulated HI discs lie on the observed mass-diameter relation (e.g. Broeils & Rhee 1997). The scatter in the mass-diameter relation and the distribution of the average HI surface density within the HI radius are also consistent with those derived for a number of observational datasets (Verheijen & Sancisi 2001; Lelli et al. 2016; Martinsson et al. 2016; Ponomareva et al. 2016).

(v) The HI gas content in the Auriga galaxies, expressed in terms of gas fractions, is a declining function of the stellar mass present in the system, in agreement with observational findings. Compared to observations, our HI fractions are at the upper end of the allowed observational range, indicating that our simulated systems are systematically more gas-rich than typical nearby galaxies.

(vi) The main results of our analysis are robust with respect to changes in the prescription used to estimate the contribution of molecular hydrogen to the total neutral hydrogen mass, although the use of the GK11 model yields HI surface densities that are lower in the central regions than those estimated via the empirical HI/H₂ mass ratio relation of L08.

(vii) Our findings are slightly sensitive to variations in numerical resolution, but we note that the results for the two finer resolution levels are in good agreement with one another. Notwithstanding that, even the simulations run at the coarsest resolution level result in systems having H I distributions whose properties are consistent with the observational trends.

Our analysis exemplifies the significant progress achieved by cosmological simulations of galaxy formation – and especially with respect to the formation of galaxies similar to our own Milky Way – which can now not only reproduce important structural properties (such as stellar masses, disc scale lengths and star formation rates) and scaling relations associated with the stellar component of late type systems, but are also able to make meaningful predictions for the (neutral) gas component within the main galaxy. The predictions of these properties can be used, in conjunction with an accurate comparison to observations, to put new and more stringent constraints to the sub-grid physics used in these calculations, which is one of the major sources of uncertainties in current cosmological simulations.

In addition, having simulated gaseous discs whose properties are in broad agreement with the observed trends in nearby disc galaxies, one can now pursue interesting new lines of research. One promising direction in the context of the H I gas would be to carry out detailed studies of its dynamical state. This is an already well established observational field in radio astronomy for which many techniques have been developed and tested. The same techniques can be now be systematically applied to simulation data, likely yielding informative comparisons between the simulated galaxies and the observations, an avenue that we intend to explore in future work.

ACKNOWLEDGEMENTS

FM thanks A. Ponomareva for helpful discussions and for kindly providing the best-fitting parameters of the observed H I mass-diameter relationship. FM is also grateful for the hospitality of the Heidelberg Institute for Theoretical studies during the final stages of this work. RG and VS acknowledge support by the DFG Research Centre SFB-881 ‘The Milky Way System’ through project A1. This work has also been supported by the European Research Council under ERC-StG grant EXAGAL- 308037. Part of the simulations of this paper used the SuperMUC system at the Leibniz Computing Centre, Garching, under the project PR85JE of the Gauss Centre for Supercomputing. All the figures in this work were produced by using the MATPLOTLIB graphics environment (Hunter 2007).

REFERENCES

Aumer M., Binney J. J., 2009, *MNRAS*, **397**, 1286
Aumer M., White S. D. M., Naab T., Scannapieco C., 2013, *MNRAS*, **434**, 3142
Bahé Y. M., et al., 2016, *MNRAS*, **456**, 1115
Barnes J., Hut P., 1986, *Nature*, **324**, 446
Battaglia G., et al., 2005, *MNRAS*, **364**, 433
Blitz L., Rosolowsky E., 2006, *ApJ*, **650**, 933
Bonatto C., Bica E., 2011, *MNRAS*, **415**, 2827
Broeils A. H., Rhee M.-H., 1997, *A&A*, **324**, 877
Catinella B., et al., 2010, *MNRAS*, **403**, 683
Catinella B., et al., 2013, *MNRAS*, **436**, 34
Chiappini C., Matteucci F., Gratton R., 1997, *ApJ*, **477**, 765

Chiappini C., Matteucci F., Romano D., 2001, *ApJ*, **554**, 1044
Colín P., Avila-Reese V., Roca-Fàbrega S., Valenzuela O., 2016, *ApJ*, **829**, 98
Crain R. A., et al., 2016, preprint, ([arXiv:1604.06803](https://arxiv.org/abs/1604.06803))
Davé R., Katz N., Oppenheimer B. D., Kollmeier J. A., Weinberg D. H., 2013, *MNRAS*, **434**, 2645
Dehnen W., McLaughlin D. E., Sachania J., 2006, *MNRAS*, **369**, 1688
Fraternali F., 2009, in Andersen J., Nordström B., Bland-Hawthorn J., eds, IAU Symposium Vol. 254, The Galaxy Disk in Cosmological Context. pp 255–262 ([arXiv:0807.3365](https://arxiv.org/abs/0807.3365)), doi:10.1017/S1743921308027671
Fraternali F., 2014, in Feltzing S., Zhao G., Walton N. A., Whitelock P., eds, IAU Symposium Vol. 298, Setting the scene for Gaia and LAMOST. pp 228–239 ([arXiv:1310.2956](https://arxiv.org/abs/1310.2956)), doi:10.1017/S1743921313006418
Fraternali F., Binney J. J., 2006, *MNRAS*, **366**, 449
Fraternali F., Binney J. J., 2008, *MNRAS*, **386**, 935
Fraternali F., Marasco A., Armillotta L., Marinacci F., 2015, *MNRAS*, **447**, L70
Giovannelli R., Haynes M. P., 2016, *A&ARv*, **24**, 1
Gnedin N. Y., Kravtsov A. V., 2011, *ApJ*, **728**, 88 (GK11)
Gómez F. A., White S. D. M., Grand R. J. J., Marinacci F., Springel V., Pakmor R., 2016a, preprint, ([arXiv:1606.06295](https://arxiv.org/abs/1606.06295))
Gómez F. A., White S. D. M., Marinacci F., Slater C. T., Grand R. J. J., Springel V., Pakmor R., 2016b, *MNRAS*, **456**, 2779
Grand R. J. J., et al., 2016a, submitted to MNRAS,
Grand R. J. J., Springel V., Gómez F. A., Marinacci F., Pakmor R., Campbell D. J. R., Jenkins A., 2016b, *MNRAS*, **459**, 199
Guedes J., Callegari S., Madau P., Mayer L., 2011, *ApJ*, **742**, 76
Habing H. J., 1968, *Bull. Astron. Inst. Netherlands*, **19**, 421
Heald G., et al., 2011, *A&A*, **526**, A118
Houck J. C., Bregman J. N., 1990, *ApJ*, **352**, 506
Hunter J. D., 2007, *Computing In Science & Engineering*, **9**, 90
Kalberla P. M. W., Burton W. B., Hartmann D., Arnal E. M., Bajaja E., Morras R., Pöppel W. G. L., 2005, *A&A*, **440**, 775
Lagos C. d. P., et al., 2015, *MNRAS*, **452**, 3815
Lelli F., McGaugh S. S., Schombert J. M., 2016, preprint, ([arXiv:1606.09251](https://arxiv.org/abs/1606.09251))
Leroy A. K., Walter F., Brinks E., Bigiel F., de Blok W. J. G., Madore B., Thornley M. D., 2008, *AJ*, **136**, 2782 (L08)
Li Y.-S., White S. D. M., 2008, *MNRAS*, **384**, 1459
Macciò A. V., Udrescu S. M., Dutton A. A., Obreja A., Wang L., Stinson G. R., Kang X., 2016, *MNRAS*, **463**, L69
Marasco A., Fraternali F., 2011, *A&A*, **525**, A134
Marasco A., Debattista V. P., Fraternali F., van der Hulst T., Wadsley J., Quinn T., Roškar R., 2015, *MNRAS*, **451**, 4223
Marasco A., Crain R. A., Schaye J., Bahé Y. M., van der Hulst T., Theuns T., Bower R. G., 2016, *MNRAS*, **461**, 2630
Marinacci F., Binney J., Fraternali F., Nipoti C., Ciotti L., Londrillo P., 2010, *MNRAS*, **404**, 1464
Marinacci F., Fraternali F., Nipoti C., Binney J., Ciotti L., Londrillo P., 2011, *MNRAS*, **415**, 1534
Marinacci F., Pakmor R., Springel V., 2014a, *MNRAS*, **437**, 1750
Marinacci F., Pakmor R., Springel V., Simpson C. M., 2014b, *MNRAS*, **442**, 3745
Marinacci F., Vogelsberger M., Mocz P., Pakmor R., 2015, *MNRAS*, **453**, 3999
Martinsson T. P. K., Verheijen M. A. W., Bershady M. A., Westfall K. B., Andersen D. R., Swaters R. A., 2016, *A&A*, **585**, A99
McCarthy I. G., Schaye J., Font A. S., Theuns T., Frenk C. S., Crain R. A., Dalla Vecchia C., 2012, *MNRAS*, **427**, 379
Navarro J. F., Steinmetz M., 1997, *ApJ*, **478**, 13
Noordermeer E., van der Hulst J. M., Sancisi R., Swaters R. A., van Albada T. S., 2005, *A&A*, **442**, 137
Oosterloo T., Fraternali F., Sancisi R., 2007, *AJ*, **134**, 1019
Pakmor R., Marinacci F., Springel V., 2014, *ApJ*, **783**, L20
Pakmor R., Springel V., Bauer A., Mocz P., Munoz D. J., Ohlmann S. T., Schaal K., Zhu C., 2016, *MNRAS*, **455**, 1134

- Peñarrubia J., Gómez F. A., Besla G., Erkal D., Ma Y.-Z., 2016, *MNRAS*, **456**, L54
- Planck Collaboration et al., 2014, *A&A*, **571**, A16
- Ponomareva A. A., Verheijen M. A. W., Bosma A., 2016, preprint, ([arXiv:1609.00378](https://arxiv.org/abs/1609.00378))
- Popping A., Davé R., Braun R., Oppenheimer B. D., 2009, *A&A*, **504**, 15
- Powell K. G., Roe P. L., Linde T. J., Gombosi T. I., De Zeeuw D. L., 1999, *Journal of Computational Physics*, **154**, 284
- Rahmati A., Pawlik A. H., Raičević M., Schaye J., 2013, *MNRAS*, **430**, 2427
- Roberts M. S., 1975, *Radio Observations of Neutral Hydrogen in Galaxies*. the University of Chicago Press, p. 309
- Sakamoto T., Chiba M., Beers T. C., 2003, *A&A*, **397**, 899
- Sancisi R., Fraternali F., Oosterloo T., van der Hulst T., 2008, *A&ARv*, **15**, 189
- Schaye J., 2001, *ApJ*, **562**, L95
- Schaye J., et al., 2015, *MNRAS*, **446**, 521
- Shapiro P. R., Field G. B., 1976, *ApJ*, **205**, 762
- Springel V., 2005, *MNRAS*, **364**, 1105
- Springel V., 2010, *MNRAS*, **401**, 791
- Springel V., Hernquist L., 2003, *MNRAS*, **339**, 289
- Springel V., et al., 2008, *MNRAS*, **391**, 1685
- Stinson G. S., Brook C., Macciò A. V., Wadsley J., Quinn T. R., Couchman H. M. P., 2013, *MNRAS*, **428**, 129
- Swaters R. A., van Albada T. S., van der Hulst J. M., Sancisi R., 2002, *A&A*, **390**, 829
- Twarog B. A., 1980, *ApJ*, **242**, 242
- Verheijen M. A. W., Sancisi R., 2001, *A&A*, **370**, 765
- Vogelsberger M., Genel S., Sijacki D., Torrey P., Springel V., Hernquist L., 2013, *MNRAS*, **436**, 3031
- Vogelsberger M., et al., 2014a, *MNRAS*, **444**, 1518
- Vogelsberger M., et al., 2014b, *Nature*, **509**, 177
- Wakker B. P., 2004, in van Woerden H., Wakker B. P., Schwarz U. J., de Boer K. S., eds, *Astrophysics and Space Science Library* Vol. 312, *High Velocity Clouds*. p. 25, doi:10.1007/1-4020-2579-3_2
- Wakker B. P., van Woerden H., 1997, *ARA&A*, **35**, 217
- Walker A. P., Gibson B. K., Pilkington K., Brook C. B., Dutta P., Stanimirović S., Stinson G. S., Bailin J., 2014, *MNRAS*, **441**, 525
- Wang J., et al., 2013, *MNRAS*, **433**, 270
- Wang J., et al., 2014, *MNRAS*, **441**, 2159
- Wang L., Dutton A. A., Stinson G. S., Macciò A. V., Penzo C., Kang X., Keller B. W., Wadsley J., 2015, *MNRAS*, **454**, 83
- Wilkinson M. I., Evans N. W., 1999, *MNRAS*, **310**, 645
- Xue X. X., et al., 2008, *ApJ*, **684**, 1143